

Terahertz pulse induced second harmonic generation and Kerr effect in the quantum paraelectric KTaO_3

Xiaojiang Li ¹, Peisong Peng ¹, Hichem Dammak ², Grégory Geneste,^{3,4} Alireza Akbarzadeh,^{5,6} Sergey Prosandeev,⁵ L. Bellaiche,⁵ and Diyar Talbayev ^{1,*}

¹*Department of Physics and Engineering Physics, Tulane University, 6400 Freret Street, New Orleans, Louisiana 70118, USA*


²*Laboratoire SPMS, Université Paris-Saclay, CentraleSupélec, CNRS, F 91190 Gif-sur-Yvette, France*

³*CEA, DAM, DIF, F-91297 Arpaçon, France*

⁴*Laboratoire Matière en Conditions Extrêmes, Université Paris-Saclay, CEA, 91680 Bruyères-le-Châtel, France*

⁵*Department of Physics, Institute for Nanoscience and Engineering, University of Arkansas, Fayetteville, Arkansas 72701, USA*

⁶*Science, Engineering, and Geosciences, LoneStar College, 9191 Barker Cypress Road, Cypress, Texas 77433, USA*

 (Received 7 November 2022; revised 9 January 2023; accepted 7 February 2023; published 21 February 2023)

We present a joint experimental and computational study of second harmonic generation and Kerr effect induced by intense terahertz electric fields in the quantum paraelectric material KTaO_3 . The single-cycle terahertz (THz) electric pulses induce the free induction decay of the polar soft phonon mode and a ferroelectric polarization response that lasts for several picoseconds in both experiment and computation. We observe a much longer-lasting (43-ps) transient Kerr effect that follows the THz excitation. We explain the disparity in the relaxation times between the THz-induced second harmonic generation and the Kerr effect by the presence of the polar nanoregions intrinsic to KTaO_3 . The origin of the slow THz Kerr effect dynamics is not presently understood. We speculate that it may be associated with the rotational motion of polar nanoregions due to the material's proximity to the ferroelectric phase transition.

DOI: [10.1103/PhysRevB.107.064306](https://doi.org/10.1103/PhysRevB.107.064306)

I. INTRODUCTION

The ultrafast optical control of ferroic orders in crystals presents both challenging fundamental questions and exciting technological opportunities [1–3]. Among the multitude of optical control schemes for various ferroic order parameters, we focus here on the control of the ferroelectric dipole moment using terahertz (THz) electric-field transients. Although other schemes for manipulating the ferroelectric order may be feasible [4–13], this method of control is appealing due to its conceptual simplicity—electric-field E couples directly to the electric dipole d via the $-dE$ energy term. The ferroelectric instability is often driven by the soft phonon mode that is resonant with the THz electric field, which means that this frequency approaches the fastest possible ferroelectric switching rates [14]. Despite a significant amount of theoretical and experimental effort in the pursuit of terahertz switching of the static ferroelectric polarization in recent years, this particular goal remains elusive.

Although the switching of the static polarization with a THz pulse has not been demonstrated yet, significant theoretical and experimental achievements took place in modeling the ferroelectric response, driving the soft-mode phonons in non-linear anharmonic regimes, and discovery of novel metastable ferroelectric states. An early theoretical proposal for THz control of ferroelectric polarization belongs to Qi *et al.*, who deployed a train of THz pulses to effect a polarization

reversal in PbTiO_3 in their molecular dynamics simulations [15]. Prosandeev and co-workers also used a THz pulse train to computationally discover hidden metastable phases and neuromorphic computing functionality in the prototype relaxor ferroelectric $\text{Pb}(\text{Mg}_{1/3}\text{Nb}_{2/3})\text{O}_3$ and in the antiferroelectric NaNbO_3 [16,17]. Zhuang and Hu discovered the significance of polarization-photon coupling in increasing the soft phonon damping in a strained single-domain ferroelectric film [18]. Experimental exploration and understanding of non-linear anharmonic phonon motion was advanced in quantum paraelectric SrTiO_3 [19,20] and in ferroelectrics BaTiO_3 and LiNbO_3 [21–23]. Large THz-induced polarization modulation and associated changes in the electronic state of the magnetic ion were reported in the ferroelectric antiferromagnet BiFeO_3 [24,25]. Modulation of the electronic states and THz-induced polar charge order was documented in organic molecular materials [26,27]. Excitation of high-frequency phonons and hidden metastable ferroelectricity driven by THz pulses were observed in quantum paraelectric SrTiO_3 [28,29].

The quantum paraelectric KTaO_3 (KTO) belongs to the perovskite family and has been intensively studied since the middle of past century [30–35]. KTO has a simple cubic structure with space-group $Pm\bar{3}m$ (No. 221) at room temperature and holds the cubic structure down to, at least, 10 K [33,36]. The quantum paraelectric state results from the competitions among antiferrodistortive structural phase transition, ferroelectric ordering, and quantum fluctuation below certain threshold temperatures [37]. The KTO single crystal exhibits many interesting physical properties, such as two-dimensional electron gas [38], superconductivity under

*dtalbayev@gmail.com

electrostatic carrier doping [39], and metal-insulator transitions [40]. Temperature-dependent dielectric constant of KTO increases continuously as the temperature drops down to 8 K and levels off toward 0 K without undergoing ferroelectric phase transition [41]. More interestingly, even though the long-range ferroelectric order is banned at low temperature, the local polar phase can still exist with $R_0/a \approx 4$ in both doped and nominally pure KTO [34,42], where a is the lattice constant and R_0 is the size of ferroelectric nanoregion. So in the low-temperature regime, the phase diagram of the KTO crystal is almost temperature independent, but very sensitive to the external stimuli, such as electromagnetic irradiation or strain. These properties make KTO an ideal material for studying nonlinear phonon dynamics and ultrafast optical control. The TO_1 soft mode in KTO can be described very well by the mean-field Barrett formula [31,43,44]. By fitting the experimental data with such a formula, Ang *et al.* found that the classical Curie temperature of KTO should be 1.6 K, the temperature at which the instability begins is 32 K, and the dielectric constant depends significantly on the external DC electric field [43].

In this article, we study both experimentally and computationally the excitation of KTO with strong THz electric-field pulses. The material's response is measured using two femtosecond optical probes: One is the THz-field-induced second harmonic generation (TFISH) [45,46], and the other is the THz-induced polarization rotation [THz Kerr effect, or (TKE)] [47,48]. We interpret the TFISH probe as the indicator of the dipolar response, which is proportional to the degree of the inversion symmetry breaking. We find that the dipolar polarization response is rather short lived and well described in the picture of effective Hamiltonians applicable to this material. Our effective Hamiltonian simulations reproduce the experimentally observed temperature dependence of the TFISH response strength and the hardening of the driven soft-mode oscillations with increasing THz peak field. We also find a novel long-lived metastable state detected via the THz Kerr effect. The discovery of this hidden metastable state opens the door for its potential applications, for example, as in novel neuromorphic computing architectures [16,17].

II. EXPERIMENTAL AND COMPUTATIONAL RESULTS

We report optical time-resolved studies of KTO where we use intense single-cycle THz pulses as the excitation. We employ optical rectification in a LiNbO_3 prism and tilted-wavefront phase matching to generate the THz pulses from femtosecond pulses with 800-nm center wavelength [49,50]. A small portion of the femtosecond pulse energy is split off before THz generation and is used as an optical probe pulse. Both the TFISH and the TKE are measured with the probe beam transmitted through the sample. For the TFISH experiment, the polarization directions of the THz pump and the optical probe pulses are both set along the [100] direction in the KTO crystal. In the TKE experiment, the THz electric field is polarized along the [100] direction, and the optical beam is polarized linearly at 45° from the THz beam. The TFISH intensity is measured using a GaP photodiode and a blue filter after the KTO sample, which eliminates the fundamental 800-nm wavelength from the detected light. The KTO sample

used here is a commercial product from MSE Supplies cut in the (100) direction with double-side polished surfaces.

A. TFISH

The KTO crystal possesses inversion symmetry so that no second harmonic generation can occur in the equilibrium state. The presence of the strong THz electric field causes a bulk polarization of the crystal, which breaks the inversion symmetry and leads to the detection of the TFISH intensity. Therefore, TFISH intensity serves as an optical probe of polarization. The TFISH intensity rises with the arrival of the THz electric field and decays within a few picoseconds after the THz pulse, Fig. 1(a). Only positive values of the TFISH intensity are recorded because it is measured as a difference in the intensity of the TFISH light with and without the THz field, and the latter intensity is zero. This is in contrast to the measurements in noncentrosymmetric media where both positive and negative TFISH intensities can be observed [45,51].

Figure 1(a) shows the temperature dependence of the time-resolved TFISH signal. The peak strength of TFISH gradually diminishes with increasing temperature. Figure 1(b) shows the corresponding frequency domain spectra of the TFISH measurement, where the Fourier transform was performed on the derivative of the time-domain signals in Fig. 1(a). The dependence of the frequency-domain spectra on the strength of the incident THz field at 15 K is shown in Fig. 1(c). The THz-field-induced second-order polarization $p^{2\omega}$ is described as a third-order nonlinear term,

$$p^{2\omega} \propto \chi^{(3)}(\omega_{\text{THz}}, \omega, \omega) E^{\text{THz}} (E^\omega)^2, \quad (1)$$

where E^{THz} denotes the THz electric field and E^ω denotes the electric field of the optical probe pulse. Our experiment measures TFISH intensity $I^{2\omega}$ that must scale as the square of the THz electric field: $I^{2\omega} \propto (p^{2\omega})^2 \propto (E^{\text{THz}})^2$. The inset in Fig. 1(c) shows the normalized peak TFISH intensity in time domain as a function of the normalized peak THz electric field. The measurements fall almost perfectly on the parabolic function, which confirms the quadratic scaling of the TFISH intensity with the THz electric field.

The observed time dependence of the TFISH signal consists of a sharp rise in intensity followed by a fast decay on which an oscillatory component is superimposed, Fig. 1(a). We interpret the oscillation as the signature of the coherent motion of the TO_1 soft phonon mode driven by the THz electric field. The TFISH intensity $I^{2\omega}$ is strongest when the phonon coordinate is at its extremal positive and negative values because this corresponds to the maximal degree of inversion symmetry breaking in the paraelectric phase of KTO. The first three peaks in TFISH intensity in Fig. 1(a) are mainly driven directly by the THz pulse packet and correspond to the extrema (positive and negative) of the THz electric field as evident from the comparison of the THz pump pulse shown as a dashed line in Fig. 1(a) with the TFISH response. The weaker TFISH oscillation that follows the first three peaks represents the free induction decay of the TO_1 soft phonon mode. The frequency-domain TFISH spectra in Fig. 1(b) peak near 2 THz, close to double the frequency of the soft mode in KTO, which is placed in the 0.53–0.65-THz range at 10 K by various measurements [31,32,41,52]. The TFISH oscillation

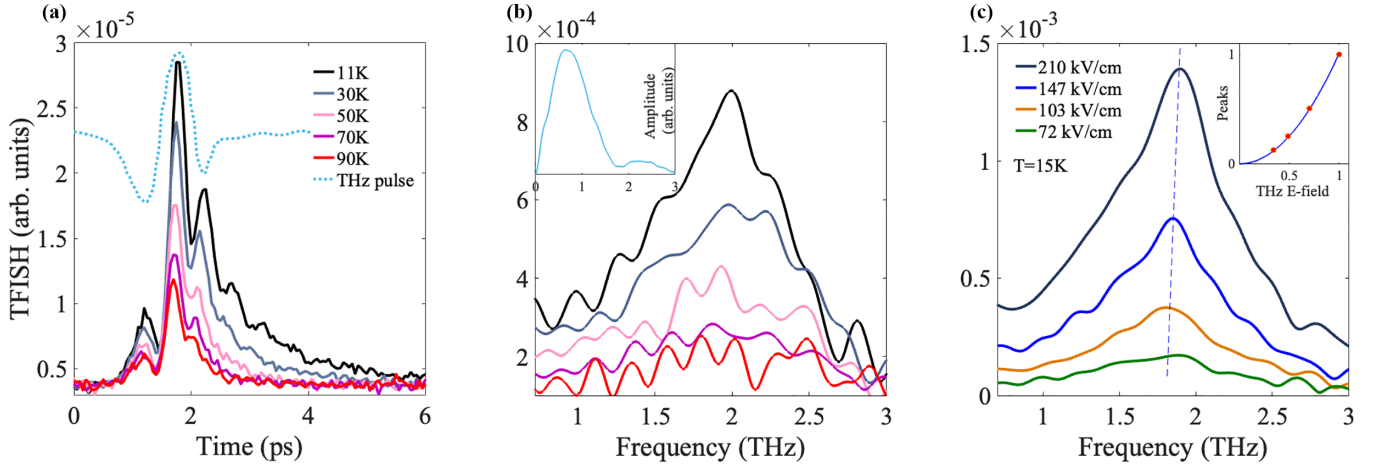


FIG. 1. THz field-induced second harmonic generation spectra. (a) Time-domain spectra under various temperatures with incident THz peak field $E = 210$ kV/cm. The dashed line shows the excitation THz pulse. (b) Frequency domain spectra corresponding to the measurements in (a). First derivatives of the interpolated time-domain spectroscopy were calculated before the Fourier transform to reduce the relative amplitude of the nonoscillatory signal. The inset: Fourier transform of the excitation THz pulse from (a). (c) Frequency domain spectra under various incident peak THz electric fields at 15 K. The inset: Peak values of TFISH time-domain spectra vs peak THz electric field. The red dots show the experimental data, and the blue solid line is the quadratic function.

occurs at double the frequency of the TO1 phonon motion because we measure the intensity of the second harmonic light, which is positive for both positive and negative phonon coordinates. The discrepancy between the cited values of the TO1 frequency in literature [31,32,41] and the TFISH frequency-domain peaks near 2 THz in Fig. 1(b) is rather high. We explain it by a combination of two factors. First, the strongest time-domain TFISH peaks represent the driven soft phonon motion and not its free oscillation. Second, when the soft mode is driven by a strong THz field to high amplitudes, a considerable hardening of the mode frequency can be expected due to the anharmonicity of the lattice potential. Indeed, our effective Hamiltonian simulations described in a later section show significant increases in the soft-mode frequency above 40-kV/cm peak THz electric field, Fig. 6(c).

B. TKE

The complementary TKE measurement is conducted right after the TFISH experiment. TKE is a third-order nonlinear optical effect that results from an additional polarization oscillating at the fundamental frequency of the probe beam [47,48],

$$p^\omega \propto \chi^{(3)}(\omega_{\text{THz}}, \omega_{\text{THz}}, \omega)(E^{\text{THz}})^2 E^\omega, \quad (2)$$

where $\chi^{(3)}(\omega_{\text{THz}}, \omega_{\text{THz}}, \omega)$ is the third-order nonlinear susceptibility. The refractive index of the specimen changes proportionally to $(E^{\text{THz}})^2$ according to Eq. (2), which leads to the polarization rotation of the probe beam E^ω . Figure 2(a) shows the temperature dependence of the time-domain TKE spectra that consist of a sharp rise and a slow decay on which an oscillatory component is superimposed. This behavior is qualitatively similar to the TFISH response in Fig. 1. In a major difference, the nonoscillatory TKE component relaxes much slower than that in TFISH measurement, specifically $\tau_{\text{TKE}} > 100$ ps at 8 K whereas $\tau_{\text{TFISH}} \sim 1$ ps at 11 K. Figure 2(b) shows the amplitude of the Fourier transform of the

derivative of the data in Fig. 2(a), whereas Fig. 2(c) displays the dependence of the frequency-domain TKE spectra on the peak strength of the incident THz field at $T = 15$ K. The frequency-domain spectra in Figs. 2(b) and 2(c) peak approximately near twice the frequency of the TO1 soft phonon mode, similar to the frequency-domain TFISH spectra. The frequency of the TKE peak increases as we increase the external field, Fig. 2(c), with a similar increase in observed in the TFISH spectra, Fig. 1(c). The inset of Fig. 2(c) displays the dependence of normalized peak TKE response on the normalized peak THz electric field, which closely follows a quadratic function. This quadratic behavior follows from the description of TKE as the third-order nonlinearity that scales as the square of the incident THz field $(E^{\text{THz}})^2$, according to Eq. (2).

Figure 2(b) shows that the oscillation in TKE is governed by the doubling of the soft mode frequency, similar to the TFISH measurements. However, the underlying mechanism of the frequency doubling is quite different. The TKE measures the change of the refractive index of the crystal, or in other words, the change in polarizability α . We can expand the polarizability as a series in normal phonon coordinates Q of the crystal [53],

$$\alpha = \alpha_0 + \sum_k \left(\frac{\partial \alpha}{\partial Q_k} \right) Q_k + \frac{1}{2} \sum_{k,k'} \left(\frac{\partial^2 \alpha}{\partial Q_k \partial Q_{k'}} \right) Q_k Q_{k'} + \dots \quad (3)$$

The linear term of Q_k in Eq. (3) is responsible for the first-order Raman scattering, whereas, the quadratic term accounts for the second-order effect. Since the KTO crystal has a cubic structure with inversion symmetry, all long-wavelength phonons at the Γ points in k space have odd parities. As a result, the first-order Raman scattering in Eq. (3) is forbidden by selection rules. The second-order Raman scattering is allowed and corresponds to the two-phonon response and results in the observed frequency-doubling behavior in our

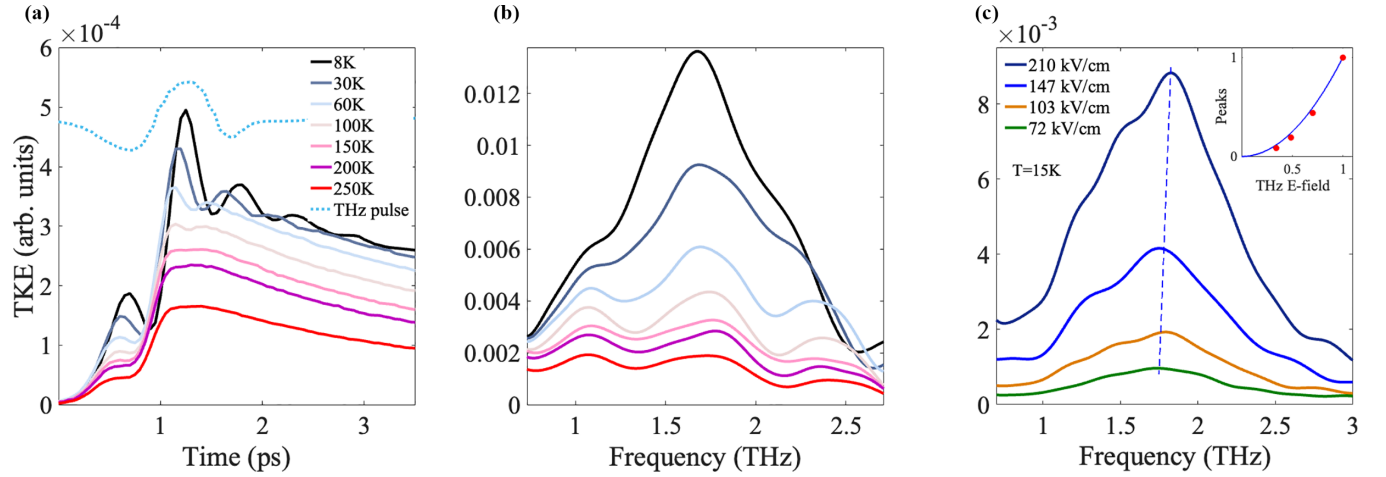


FIG. 2. THz field-induced Kerr effect spectra. (a) Time-domain TKE spectra under various temperatures with the incident THz peak field of $E = 210$ kV/cm. (b) The frequency domain spectra corresponding to the measurements in (a). (c) Frequency domain spectra under various incident THz electric field at 15 K. The inset: the peak values of TKE time-domain spectra vs peak THz electric field, red dots are the experimental data, and the blue solid line is the quadratic function.

TKE measurement [35,54]. As with TFISH, the frequency doubling is not exact due to the hardening of the soft-mode frequency when it is driven to high amplitudes by strong THz fields.

Figure 3 shows the TKE measurements extended to long probe delay times. The oscillatory component at early time delays is not visible because of a long-time step used in the collection of data in the figure. We observe that the TKE signal at low temperatures persists for over 100 ps. The small jumps at 31 ps are due to a copy of the main pump pulse from the reflection on the surfaces of a silicon wafer placed in the THz beam path as a filter. We used the biexponential function,

$$f = A \exp\left(\frac{-(t-t_0)}{\tau_1}\right) + B \exp\left(\frac{-(t-t_0)}{\tau_2}\right), \quad (4)$$

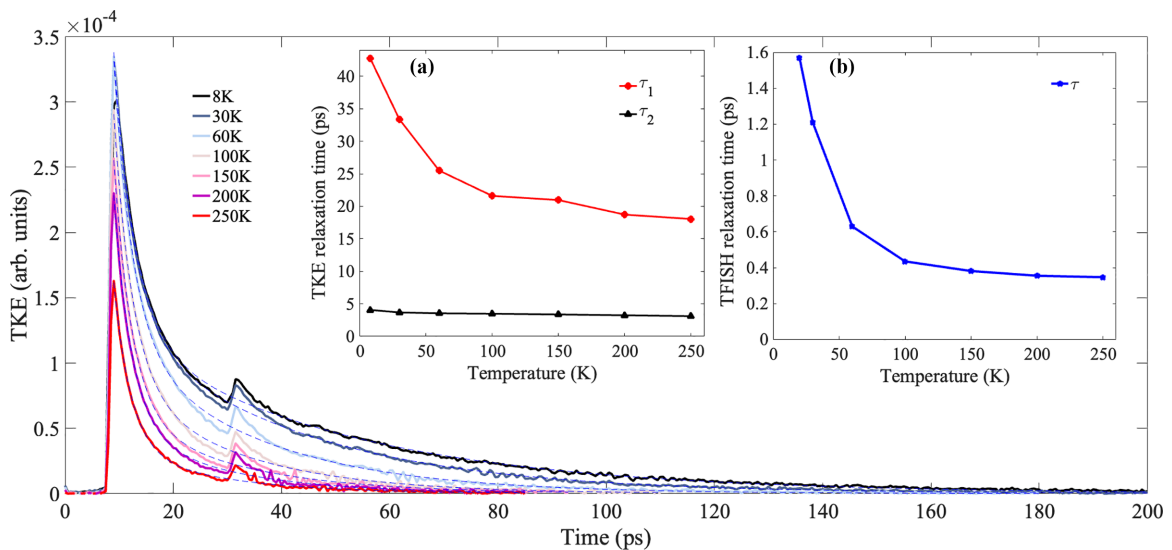


FIG. 3. Long-time range THz field-induced Kerr effect spectra with incident THz peak field $E = 210$ kV/cm. The main figure shows long-time domain TKE spectra vs temperature. The dashed blue lines are the fitting curves with the biexponential function: $f = Ae^{-\frac{(t-t_0)}{\tau_1}} + Be^{-\frac{(t-t_0)}{\tau_2}}$. The inset (a) shows the extracted relaxation times. The inset (b) shows the relaxation times from TFISH measurements extracted using the exponential function: $f = Ae^{-\frac{(t-t_0)}{\tau}}$.

to fit the relaxation behavior and determine the relaxation times τ_1 and τ_2 plotted in the inset (a) of Fig. 3. The shorter relaxation time τ_2 in black triangles behaves more like a constant with the value about 4 ps, whereas the relaxation time τ_1 in red closed circles is much larger than τ_2 and increases from 18 to 43 ps as the temperature decreases. As a comparison, we also plotted the relaxation time τ from TFISH measurement in inset (b) of Fig. 3. The relaxation time from TFISH increases relatively faster than τ_1 of TKE, from 0.35 to 1.57 ps.

C. Simulation

We performed simulations to better understand the effect of the temperature and the peak electric field of the THz pump pulse on the measured TFISH response. We used the effective

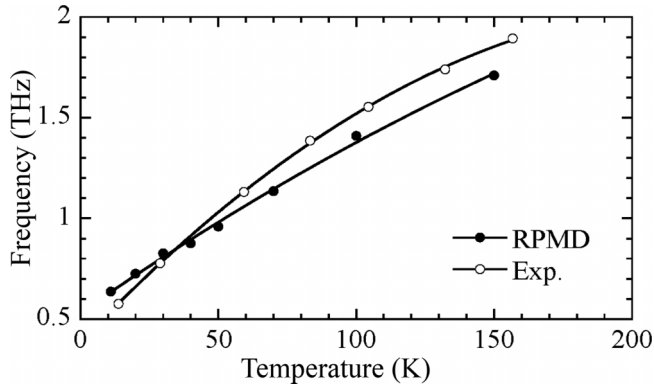


FIG. 4. Frequency of the polar mode as a function of temperature obtained by RPMD simulations. Experimental results are those from Ref. [49].

Hamiltonian developed by Akbarzadeh *et al.* [55] and applied the ring polymer molecular-dynamics (RPMD) method [56] to take into account the nuclear quantum effects. This Hamiltonian had been used to reproduce the quantum paraelectric behavior of KTO by the path-integral Monte Carlo method using a product $PT = 600$, where P is the so-called Trotter number and T is the temperature [55]. In the present simulation, the soft-mode mass is slightly modified so that the frequency of the TO_1 mode is the closest to the experimentally measured one in the 10–150-K temperature range (Fig. 4). It is chosen equal to $m = 80 \text{ g mol}^{-1}$ instead of 95.6 g mol^{-1} . Indeed, the experimental value of this frequency at 20 K is equal to 0.66 THz, and calculations give values equal to 0.45 and 0.67 THz for an effective mass equal to 95.6 and 80 g/mol,

respectively. Note that the frequency ratio (1.49) differs from the inverse of the square root of the mass ratio (1.09). This is due to the anharmonicity of the potential and nuclear quantum effects. The inhomogeneous-deformation mode mass equals the KTaO_3 “molecule” mass, and the product PT is equal to 1280. KTO is simulated in the isothermal-isobaric ensemble by using the extended Langevin thermostat [57,58] that was previously implemented to study barium titanate [59]. The MD simulations are performed using $N = 12 \times 12 \times 12$ cells with periodic boundary conditions. The time step is 0.4 fs. The friction coefficient of the Langevin thermostat and barostat is 0.2 THz and the mass associated with the barostat is equal to $0.5 \times 10^{-41} \text{ J s}^2$.

To calculate the frequency of the TO mode, we first determined the effective-potential energy vs reduced polarization curve at $T = 20 \text{ K}$ using the method based on the integration of the average force under constrained polarization [60]. Figure 5(a) shows the curves obtained for a polarization along the [100] direction that can be fitted using the following expression:

$$V(u) = a_0^2 \left(\frac{1}{2} k u^2 + \frac{1}{4} b u^4 + \frac{1}{6} c u^6 \right), \quad (5)$$

where $a_0 = 0.398 \text{ nm}$ is the cell parameter, u is the reduced soft-mode coordinate, $k = 2.30 \pm 0.01$, $b = (7.7 \pm 0.3) \times 10^3$, and $c = (5.5 \pm 0.1) \times 10^7 \text{ N/m}$. The derived frequency $\frac{1}{2\pi} \sqrt{k/m}$ is equal to 0.67 THz, which is close to the reported experimental values [31,32,41,52].

Moreover, the RPMD method allows the calculation of temporal correlation functions in a satisfactory way for a short duration of a few oscillations [61]. We used it to predict the frequency of the TO_1 mode from the position of the peak of the imaginary susceptibility according to the following

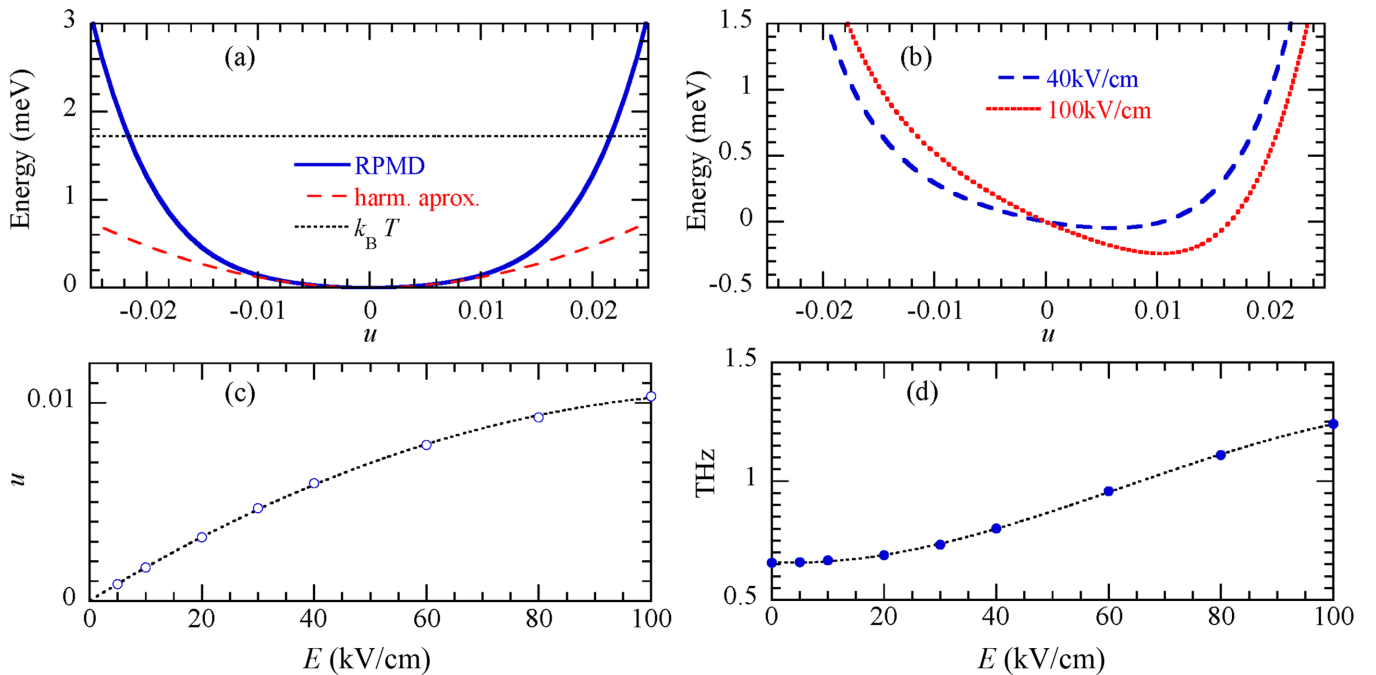


FIG. 5. RPMD simulations at 20 K. (a) Effective energy-potential $V(u)$ as a function of the reduced polarization along the [100] direction (blue line) and its harmonic approximation curve (red dashed line). The thermal energy $k_B T$ level is shown by the black dotted line. (b) Example of curves $V(u) - E u$ under a static electric field E . (c) Induced polarization as a function of E . (d) frequency of the polar mode (TO) as derived in the harmonic approximation close to the minimum of the $V(u) - E u$ curve.

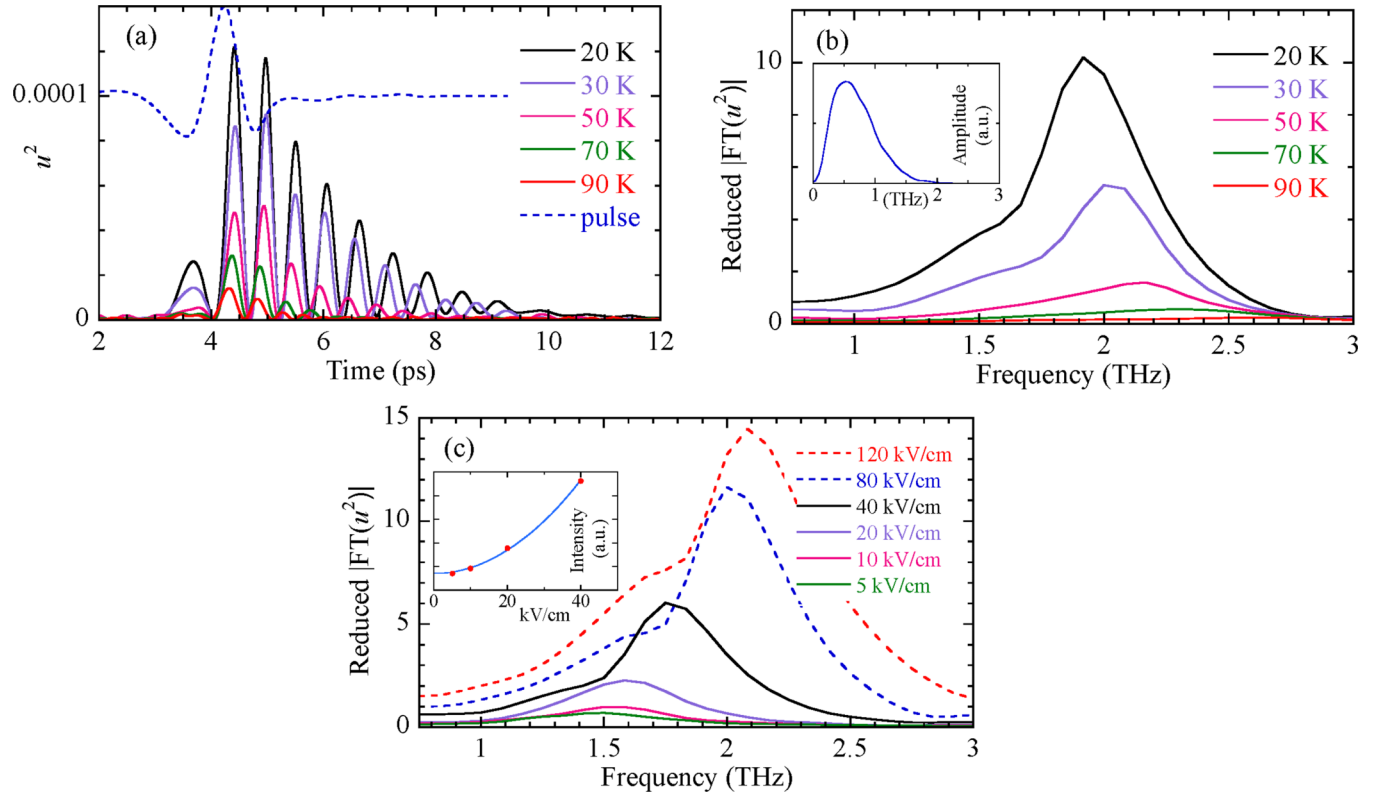


FIG. 6. Computed dielectric response of KTO to a realistic time-domain THz pulse with an electric field parallel to [100]: panel (a) shows the square of the induced polarization u^2 (reduced unit) as a function of time in the case of $E_{\max} = 60$ kV/cm. The realistic THz-field pulse used for the calculation is shown by the dashed blue line. Panels (b) and (c) show the reduced Fourier transform (FT) amplitude of u^2 in the 0–12-ps range, according to the expression (8). Panel (b) is for $E_{\max} = 60$ kV/cm whereas panel (c) is for different E_{\max} 's for 20 K. The inset in panel (b) shows the FT amplitude of the pulse. The inset in panel (c) shows the integrated intensity in the 0.5–5-THz range and its quadratic fit.

expression [62]:

$$\chi''(\omega) = \left(\frac{\beta \hbar \omega}{1 - e^{-\beta \hbar \omega}} \right) \frac{1}{V 3 \epsilon_0 k_B T} \times \text{Re} \left[\omega \int_{-\infty}^{+\infty} e^{i\omega t} \langle \mathbf{P}(0) \cdot \mathbf{P}(t) \rangle dt \right], \quad (6)$$

where $\mathbf{P} = Z^* e a_0 \sum_{i=1}^N \mathbf{u}_i$ is the total electric dipole moment of the system, $V = N a_0^3$ is its volume, $Z^* e$ is the effective charge of the soft mode, a_0 is the cell parameter, and \mathbf{u}_i is the reduced polarization of the i th cell. In practice, it is useful to calculate χ'' using the following approximation for a time length of τ :

$$\chi''(\omega) \simeq \left(\frac{\beta \hbar \omega}{1 - e^{-\beta \hbar \omega}} \right) \frac{1}{V 3 \epsilon_0 k_B T} \frac{\omega}{\tau} \left| \int_0^\tau e^{i\omega t} \mathbf{P}(t) dt \right|^2. \quad (7)$$

At $T=20$ K under no field, the peak is at 0.64 ± 0.02 THz, which is a value very close to the one deduced from the effective potential. This comparison shows us that we can follow the system's dynamics over several picoseconds to study the response of KTO to the pulse. Figure 4 shows that the present effective Hamiltonian and the RPMD method capture with very good accuracy the experimental-temperature dependence of the soft-mode's frequency in KTO [31,32,41,52].

To choose the amplitude values of the pulse's electric field, we have determined the induced polarization as a function

of the external field E , which corresponds to the position of the curve minimum of the $V(u) - Eu$ function, Fig. 5(b). Figure 5(c) shows that at 20 K, the simulated response remains linear for a field below about 40 kV/cm.

We simulated the ferroelectric response of KTO using a realistic time-domain THz pulse. For a given temperature and a given peak field of the THz pulse (E_{\max}^{THz}), the curves of Fig. 6 are obtained by averaging through six independent trajectories. Since the intensity measured during the TFISH experiments appears proportional to $(E_{\max}^{\text{THz}})^2$, we focus on the square of the polarization induced by the pulse u^2 assuming that the response is quasilinear, Fig. 6(a). In addition, the Fourier transform amplitude of u^2 is reduced by using the following expression:

$$\frac{1}{V 3 \epsilon_0 k_B T} \frac{\omega}{\tau} \left| \int_0^\tau e^{i\omega t} \mathbf{p}^2(t) dt \right|, \quad (8)$$

where $\mathbf{p} = Z^* e a_0 \mathbf{u}$ is the average polarization per unit cell, and $\tau = 12$ ps.

Figure 6(b) shows that the peak Fourier-transform frequency increases with increasing temperature. According to Fig. 4, this behavior is expected since this frequency is assumed to be the second harmonic of the TO_1 soft mode. However, the value of this frequency at 20 K, for example, is equal to 1.94 ± 0.02 THz for $E_{\max}^{\text{THz}} = 60$ kV/cm, and it is higher than twice the frequency of the TO_1 mode, i.e.,

1.34 THz for zero field, Fig. 4. This difference occurs because the strong THz electric field drives the soft-mode coordinate into the anharmonic regime where the restoring force near the extremal points of the phonon motion exceeds the harmonic restoring force, Fig. 5(a). The resulting anharmonic hardening of the soft-mode frequencies is observed in the simulation results of Fig. 6(b) as well as the TFISH and TKE experiments of Figs. 1 and 2. Figure 6(c) shows the simulated dependence of the THz-driven soft-mode oscillations and their frequency on the peak field strength, which qualitatively reproduces the measured dependence in TFISH and TKE, Figs. 1(c) and 2(c).

To better understand the discrepancy between the measured and the computed soft-mode frequencies, we first point out that the field values cited in Figs. 1–3 are peak incident THz fields. When the incident THz field enters the KTO bulk through the surface, the electric field is reduced by the factor equal to the Fresnel transmission coefficient equal to $2/(n + 1)$ for normal incidence. For $T = 20$ K, the refractive index [41] $n = 55$, reducing the maximum incident 210-kV/cm electric field to 7.5 kV/cm inside KTO. In computation, the electric fields cited in Figs. 5 and 6 are internal electric fields in the material. The highest TFISH oscillation frequency of 1.9 THz is observed at the peak incident field of 210 kV/cm (7.5 kV/cm internal peak field) in the experiment, Fig. 1(c). In computation, a comparable effect on the soft-mode frequency is induced by the 80-kV/cm peak internal field, Fig. 6(c). Therefore, the computation overestimates the experimental electric field by about an order of magnitude. This situation is common in effective Hamiltonian simulations of ferroelectric and related materials and is known as the Landauer paradox [63], which arises due to the contribution of the depolarizing field to the domain activation energy, making this activation significantly higher than observed in experiments.

We offer another interpretation of the effect of the strong THz electric field on the observed soft-mode frequencies. Indeed, given the large ratio of the optical frequency used to probe the induced polarization and that of the pulse (375/1 THz), we can view KTO as being subjected to a static electric field at the timescale of the intensity measurement (0.1 ps). The harmonic approximation of the modified effective potential $V(u) - Eu$, Fig. 5(b), then allows to estimate the frequency of the TO_1 mode as a function of E . According to Fig. 5(d), the second harmonic of the TO_1 mode at 60 kV/cm would correspond to 1.916 THz, which is in remarkable agreement with the value found in Fig. 6(b). Similarly, the dependence of the peak frequency with increasing pulse amplitude in Fig. 6(c) follows the dependence of the soft-mode frequency on the applied static electric field shown in Fig. 5(d).

III. DISCUSSION

By far, the most striking observation from the two complementary measurements TFISH and TKE is the order-of-magnitude difference between the nonoscillatory relaxation time τ_1 of TKE and τ of TFISH. The relaxation times for TKE are more than 20 times larger than TFISH from close to room temperature down to 8 K, Fig. 3. This difference is even more puzzling when the TFISH and TKE relaxation times are compared with the free induction decay time of

the soft phonon mode, which was measured by THz and hyper-Raman spectroscopy [41,64]. The soft-mode damping constant $\gamma/2\pi = 0.06$ THz in the 10–50-K range, and corresponding free induction decay time $2\tau = 2/\gamma = 5.3$ ps. The decay time of the square of the soft phonon mode coordinate $u^2(t)$ is $\tau = 2.7$ ps. The latter number is of the comparable order of magnitude, but still much higher than the measured TFISH relaxation time 0.6–1.6 ps in the 10–50 K range, Fig. 3. The phonon free induction decay time is also more than an order of magnitude lower than our measured relaxation time of TKE. This raises the question of the origin of the observed TFISH and TKE relaxation times.

The shorter relaxation time of TFISH compared to the phonon free induction decay can be explained by postulating the presence of an inhomogeneity in the material. Experimental and theoretical evidence suggest the existence of polar micro- or nanoregions in an overall paraelectric KTaO_3 crystal [34,55]. Let us label the spontaneous polarization of such polar micro/nanoregions as P_i . There is no macroscopic polarization, so we set $\sum_i P_i = 0$, where the index i runs over all polar regions (PRs). The THz pulse induces linear polarization p_i in each PR. (For simplicity, P_i and p_i denote the scalar components of the three-dimensional polarization vectors along the direction of the THz electric field.) The presence of both P_i and p_i allow optical second-order polarization and SHG when a fundamental optical wave E^ω with intensity I^ω traverses the KTO crystal. From this perspective, earlier Eq. (1) can be rewritten as

$$p_i^{2\omega} \propto [\alpha(P_i + p_i)](E^\omega)^2 \propto (P_i + p_i)I^\omega, \quad (9)$$

where α is the hyper-Raman tensor [65]. The total intensity $I^{2\omega}$ of the emitted second harmonic light is due to the macroscopic second-order polarization that can be obtained after summing over all PRs,

$$I^{2\omega} \propto \left(\sum_i (P_i + p_i) \right)^2 (I^\omega)^2. \quad (10)$$

In our TFISH experiments, we measure the difference between the second harmonic intensity with and without the THz pulse,

$$\begin{aligned} I^{\text{TFISH}} &\propto \left[\left(\sum_i (P_i + p_i) \right)^2 - \left(\sum_i P_i \right)^2 \right] (I^\omega)^2 \\ &= \left[2 \left(\sum_i P_i \right) \left(\sum_i p_i \right) + \left(\sum_i p_i \right)^2 \right] (I^\omega)^2. \end{aligned} \quad (11)$$

Because $\sum_i P_i = 0$, we find

$$I^{\text{TFISH}} \propto \left[\sum_i p_i^2 + 2 \sum_{i \neq j} p_i p_j \right] (I^\omega)^2. \quad (12)$$

The quantity in the square brackets is dominated by the second summation of the products $p_i p_j$ because the first sum in brackets contains vanishingly fewer terms compared to the second sum (in a $p_i p_j$ matrix, the first sum is the sum of the diagonal elements, and the second sum is the sum of all other elements in the matrix) and because the THz-induced polarizations p_i

in each PR start their time evolution in phase with each other after the excitation by the THz pulse. Hence, the second sum in brackets in Eq. (12) will determine the time evolution of the TFISH signal. If there exists an inhomogeneity that results in a fast dephasing of the induced polarizations between different PRs, then TFISH intensity in Eq. (12) can decay in time faster than the decay of the squares of individual polarizations p_i^2 . Thus, the faster relaxation of the TFISH intensity compared with the phonon free induction decay can be the result of an intrinsic inhomogeneity in the material, although our measurement does not establish the nature of the inhomogeneity.

On the other hand, TKE results from the third-order nonlinear polarization that scales as $(E^{\text{THz}})^2$, Eq. (2). In a homogeneous medium of length L [47], the intensity of the TKE signal is related to the change in refractive index Δn caused by the application of THz electric field: $I^{\text{TKE}} = (\Delta n \omega L/c) I^\omega$. In an inhomogeneous medium with PRs carrying spontaneous polarizations P_i , as above, the refractive index change Δn_i in each PR contributes to the TKE intensity,

$$I^{\text{TKE}} \propto \left(\sum_i \Delta n_i \right) I^\omega. \quad (13)$$

The dependence of refractive index on the electric polarization can be written as $n_i = n_0 + n'_2(P_i + p_i)^2$, where the polarization p_i is induced by the THz electric field. Then

$$I^{\text{TKE}} \propto n'_2 \left[\sum_i (P_i + p_i)^2 - P_i^2 \right] I^\omega = n'_2 \left[\sum_i 2P_i p_i + p_i^2 \right] I^\omega, \quad (14)$$

where the sum in the square brackets is dominated by the second term because $\sum_i P_i = 0$. Thus,

$$I^{\text{TKE}} \propto n'_2 \left[\sum_i p_i^2 \right] I^\omega. \quad (15)$$

Comparing Eqs. (12) and (15), we observe that the inhomogeneous dephasing term containing the products $p_i p_j$ with $i \neq j$ is absent from the TKE intensity, unlike the TFISH intensity. The absence of the inhomogeneous dephasing term in Eq. (15) means that the TKE relaxation time can be much longer than the TFISH relaxation time as found in the experiment. [We note that the initial in-phase motions of polarizations p_i result in the coherent oscillation of the TKE intensity observed in experiment during the first 1 to 2 ps, Fig. 2, which is superimposed on the long-lived exponential background resulting from the incoherent contributions of PRs to the sum in Eq. (15).] The TKE relaxation time can be even longer than the phonon decay times measured by THz spectroscopy [41] because the latter measurement includes the inhomogeneous

broadening. Nevertheless, the nearly order-of-magnitude difference at low temperature between the measured phonon decay times [41,64] ($2\tau = 2/\gamma = 5.3$ ps) and the TKE relaxation time, Fig. 3, remains remarkable. Our measurement does not identify the mechanism for such slow THz-induced dynamics. If allowed to speculate, we can borrow the notion of molecular orientational relaxation in liquids [47] and associate it with the orientational motion of PRs. This nematic orientation occurs along or opposite the direction of the applied THz field, as suggested by its coupling to the square of the field, $(E^{\text{THz}})^2$, and is characterized by the very long measured relaxation times, Fig. 3. This long-lived metastable state can be classified as a hidden THz-induced phase in KTO as it is not accessible by other thermodynamic routes.

IV. SUMMARY

We studied the response of quantum paraelectric KTaO_3 to intense THz pulses experimentally using the complimentary TFISH and TKE measurements and computationally using effective Hamiltonian methods. We observed the coherent excitation of the soft phonon mode in the material with both experiment and computation. In computation, we observed the increase in the frequency of the soft mode with the THz peak field strength. The computation largely reproduces the experimental observations with TFISH. Most strikingly, we found dramatically different relaxation times for the TFISH and TKE responses in the experiment. We show that the short relaxation of the TFISH can result from intrinsic inhomogeneity in KTO, such as from the previously suggested polar nanoregions [34,55]. The TKE measurement is insensitive to this inhomogeneity, which partially explains the disparity in the TFISH and TKE relaxation times. We also propose that other slower dynamics may be contributing to the long-lived THz-induced polarization rotation. Very speculatively, such dynamics can be associated with the orientational motion of the polar nanoregions, which exist due to the material's proximity to the ferroelectric phase transition [55]. The persistent state observed via TKE can be categorized as a hidden metastable phase [29] with prospective novel applications in THz frequency electronics [16,17].

ACKNOWLEDGMENTS

The work at Tulane was supported by the National Science Foundation under Grant No. DMR-1554866. A.A. and L.B. thank the MonArk NSF Quantum Foundry supported by the National Science Foundation Q-AMASE-i Program under NSF Award No. DMR-1906383. S.P. and L.B. also acknowledge ONR Grant No. N00014-21-1-2086 and the Vannevar Bush Faculty Fellowship (VBFF) Grant No. N00014-20-1-2834 from the Department of Defense.

- [1] P. Salen, M. Basini, S. Bonetti, J. Hebling, M. Krasilnikov, A. Y. Nikitin, G. Shamuilov, Z. Tibai, V. Zhaunerchyk, and V. Goryashko, *Phys. Rep.* **836-837**, 1 (2019).
 [2] A. V. Kimel, A. M. Kalashnikova, A. Pogrebna, and A. K. Zvezdin, *Phys. Rep.* **852**, 1 (2020)

- [3] A. de la Torre, D. M. Kennes, M. Claassen, S. Gerber, J. W. McIver, and M. A. Sentef, *Rev. Mod. Phys.* **93**, 041002 (2021).
 [4] K. A. Brekhov, K. A. Grishunin, D. V. Afanas'ev, S. V. Semin, N. E. Sherstyuk, G. K. Kitaeva, E. D. Mishina, T. Rasing, and A. V. Kimel, *JETP Lett.* **102**, 372 (2015).

- [5] R. Mankowsky, A. von Hoegen, M. Först, and A. Cavalleri, *Phys. Rev. Lett.* **118**, 197601 (2017).
- [6] C. Lian, Z. A. Ali, H. Kwon, and B. M. Wong, *J. Phys. Chem. Lett.* **10**, 3402 (2019).
- [7] T. F. Nova, A. S. Disa, M. Fechner, and A. Cavalleri, *Science* **364**, 1075 (2019).
- [8] A. S. Disa, T. F. Nova, and A. Cavalleri, *Nat. Phys.* **17**, 1087 (2021).
- [9] M. Henstridge, M. Foerst, E. Rowe, M. Fechner, and A. Cavalleri, *Nat. Phys.* **18**, 457 (2022).
- [10] Y. Zhang, J. Dai, X. Zhong, D. Zhang, G. Zhong, and J. Li, *Adv. Sci.* **8**, 2102488 (2021).
- [11] J. Guo, W. Chen, H. Chen, Y. Zhao, F. Dong, W. Liu, and Y. Zhang, *Adv. Opt. Mater.* **9**, 2002146 (2021).
- [12] Q. Guo, R. Sekine, L. Ledezma, R. Nehra, D. J. Dean, A. Roy, R. M. Gray, S. Jahani, and A. Marandi, *Nat. Photonics* **16**, 625 (2022).
- [13] V. Krapivin, M. Gu, D. Hickox-Young, S. W. Teitelbaum, Y. Huang, G. de la Peña, D. Zhu, N. Sirica, M. C. Lee, R. P. Prasankumar, A. A. Maznev, K. A. Nelson, M. Chollet, J. M. Rondinelli, D. A. Reis, and M. Trigo, *Phys. Rev. Lett.* **129**, 127601 (2022).
- [14] E. Mishina, V. Bilyk, N. Sherstyuk, and A. Sigov, *Ferroelectrics* **577**, 1 (2021).
- [15] T. Qi, Y.-H. Shin, K.-L. Yeh, K. A. Nelson, and A. M. Rappe, *Phys. Rev. Lett.* **102**, 247603 (2009).
- [16] S. Prosandeev, J. Grollier, D. Talbayev, B. Dkhil, and L. Bellaïche, *Phys. Rev. Lett.* **126**, 027602 (2021).
- [17] S. Prosandeev, S. Prokhorenko, Y. Nahas, Y. Yang, C. Xu, J. Grollier, D. Talbayev, B. Dkhil, and L. Bellaïche, *Phys. Rev. B* **105**, L100101 (2022).
- [18] S. Zhuang and J.-M. Hu, *Phys. Rev. B* **106**, L140302 (2022).
- [19] I. Katayama, H. Aoki, J. Takeda, H. Shimosato, M. Ashida, R. Kinjo, I. Kawayama, M. Tonouchi, M. Nagai, and K. Tanaka, *Phys. Rev. Lett.* **108**, 097401 (2012).
- [20] S. Pal, N. Strkalj, C.-J. Yang, M. C. Weber, M. Trassin, M. Woerner, and M. Fiebig, *Phys. Rev. X* **11**, 021023 (2021).
- [21] F. Chen, Y. Zhu, S. Liu, Y. Qi, H. Y. Hwang, N. C. Brandt, J. Lu, F. Quirin, H. Enquist, P. Zalden, T. Hu, J. Goodfellow, M. J. Sher, M. C. Hoffmann, D. Zhu, H. Lemke, J. Glowina, M. Chollet, A. R. Damodaran, J. Park, Z. Cai, I. W. Jung, M. J. Highland, D. A. Walko, J. W. Freeland, P. G. Evans, A. Vaillonis, J. Larsson, K. A. Nelson, A. M. Rappe, K. Sokolowski-Tinten, L. W. Martin, H. Wen, and A. M. Lindenberg, *Phys. Rev. B* **94**, 180104(R) (2016).
- [22] K. A. Grishunin, N. A. Ilyin, N. E. Sherstyuk, E. D. Mishina, A. Kimel, V. M. Mukhortov, A. V. Ovchinnikov, O. V. Chefonov, and M. B. Agranat, *Sci. Rep.* **7**, 687 (2017).
- [23] B. E. Knighton, R. T. Hardy, C. L. Johnson, L. M. Rawlings, J. T. Woolley, C. Calderon, A. Urrea, and J. A. Johnson, *J. Appl. Phys.* **125**, 144101 (2019).
- [24] F. Chen, J. Goodfellow, S. Liu, I. Grinberg, M. C. Hoffmann, A. R. Damodaran, Y. Zhu, P. Zalden, X. Zhang, I. Takeuchi *et al.*, *Adv. Mater.* **27**, 6371 (2015).
- [25] N. Sono, Y. Kinoshita, N. Kida, T. Ito, H. Okamoto, and T. Miyamoto, *J. Phys. Soc. Jpn.* **90**, 033703 (2021).
- [26] K. Asada, T. Miyamoto, H. Yamakawa, J. Hirata, N. Takamura, T. Morimoto, K. Suzuki, T. Otaki, N. Kida, T. Nakamura *et al.*, *Phys. Rev. B* **104**, 195148 (2021).
- [27] H. Yamakawa, T. Miyamoto, T. Morimoto, N. Takamura, S. Liang, H. Yoshimochi, T. Terashige, N. Kida, M. Suda, H. M. Yamamoto *et al.*, *Nat. Commun.* **12**, 953 (2021).
- [28] M. Kozina, M. Fechner, P. Marsik, T. van Driel, J. M. Glowina, C. Bernhard, M. Radovic, D. Zhu, S. Bonetti, U. Staub *et al.*, *Nat. Phys.* **15**, 387 (2019).
- [29] X. Li, T. Qiu, J. Zhang, E. Baldini, J. Lu, A. M. Rappe, and K. A. Nelson, *Science* **364**, 1079 (2019).
- [30] R. C. Miller and W. G. Spitzer, *Phys. Rev.* **129**, 94 (1963).
- [31] H. Vogt and H. Uwe, *Phys. Rev. B* **29**, 1030 (1984).
- [32] P. A. Fleury and J. M. Worlock, *Phys. Rev.* **174**, 613 (1968).
- [33] G. Shirane, R. Nathans, and V. J. Minkiewicz, *Phys. Rev.* **157**, 396 (1967).
- [34] H. Uwe, K. B. Lyons, H. L. Carter, and P. A. Fleury, *Phys. Rev. B* **33**, 6436 (1986).
- [35] C. H. Perry, J. H. Fertel, and T. F. McNelly, *J. Chem. Phys.* **47**, 1619 (1967).
- [36] C. H. Perry, R. Currat, H. Buhay, R. M. Migoni, W. G. Stirling, and J. D. Axe, *Phys. Rev. B* **39**, 8666 (1989).
- [37] U. Aschauer and N. A. Spaldin, *J. Phys.: Condens. Matter* **26**, 122203 (2014).
- [38] P. D. C. King, R. H. He, T. Eknapakul, P. Buaphet, S.-K. Mo, Y. Kaneko, S. Harashima, Y. Hikita, M. S. Bahramy, C. Bell *et al.*, *Phys. Rev. Lett.* **108**, 117602 (2012).
- [39] K. Ueno, S. Nakamura, H. Shimotani, H. T. Yuan, N. Kimura, T. Nojima, H. Aoki, Y. Iwasa, and M. Kawasaki, *Nat. Nanotechnol.* **6**, 408 (2011).
- [40] Y. Yang, C.-S. Lin, J.-F. Chen, L. Hu, and W.-D. Cheng, *J. Appl. Phys.* **116**, 153709 (2014).
- [41] Y. Ichikawa, M. Nagai, and K. Tanaka, *Phys. Rev. B* **71**, 092106 (2005).
- [42] Y. Uesu, R. Nakai, J.-M. Kiat, C. Ménoiret, M. Itoh, and T. Kyomen, *J. Phys. Soc. Jpn.* **73**, 1139 (2004).
- [43] C. Ang, A. S. Bhalla, and L. E. Cross, *Phys. Rev. B* **64**, 184104 (2001).
- [44] K. A. Müller and H. Burkard, *Phys. Rev. B* **19**, 3593 (1979).
- [45] A. Nahata and T. F. Heinz, *Opt. Lett.* **23**, 67 (1998).
- [46] D. J. Cook, J. X. Chen, E. A. Morlino, and R. M. Hochstrasser, *Chem. Phys. Lett.* **309**, 221 (1999).
- [47] M. C. Hoffmann, N. C. Brandt, H. Y. Hwang, K.-L. Yeh, and K. A. Nelson, *Appl. Phys. Lett.* **95**, 231105 (2009).
- [48] S. Lin, S. Yu, and D. Talbayev, *Phys. Rev. Appl.* **10**, 044007 (2018).
- [49] J. Hebling, G. Almási, I. Z. Kozma, and J. Kuhl, *Opt. Express* **10**, 1161 (2002).
- [50] H. Hirori, A. Doi, F. Blanchard, and K. Tanaka, *Appl. Phys. Lett.* **98**, 091106 (2011).
- [51] J. Chen, P. Han, and X.-C. Zhang, *Appl. Phys. Lett.* **95**, 011118 (2009).
- [52] H. Vogt, *Phys. Rev. B* **41**, 1184 (1990).
- [53] G. Turrel, *Infrared and Raman Spectra of Crystals*, Spectroscopy and Spectrum Analysis (Academic, London/New York, 1972).
- [54] M. A. Allodi, I. A. Finneran, and G. A. Blake, *J. Chem. Phys.* **143**, 234204 (2015).
- [55] A. R. Akbarzadeh, L. Bellaïche, K. Leung, J. Íñiguez, and D. Vanderbilt, *Phys. Rev. B* **70**, 054103 (2004).
- [56] I. R. Craig and D. E. Manolopoulos, *J. Chem. Phys.* **121**, 3368 (2004).

- [57] D. Quigley and M. I. J. Probert, *J. Chem. Phys.* **120**, 11432 (2004).
- [58] D. Quigley and M. Probert, *Comput. Phys. Commun.* **169**, 322 (2005).
- [59] G. Geneste, H. Dammak, M. Hayoun, and M. Thiercelin, *Phys. Rev. B* **87**, 014113 (2013).
- [60] G. Geneste, *Comput. Phys. Commun.* **181**, 732 (2010).
- [61] A. Pérez, M. E. Tuckerman, and M. H. Müser, *J. Chem. Phys.* **130**, 184105 (2009).
- [62] R. Kubo, M. Toda, and N. Hashitsume, *Statistical Physics II: Nonequilibrium Statistical Mechanics* (Springer, Berlin, 2012), Vol. 31.
- [63] S. Prosandeev, and L. Bellaiche, *Phys. Rev. Mater.* **6**, 116201 (2022).
- [64] H. Vogt, *Phys. Rev. B* **51**, 8046 (1995).
- [65] A. M. Pugachev, V. I. Kovalevskii, N. V. Surovtsev, S. Kojima, S. A. Prosandeev, I. P. Raevski, and S. I. Raevskaya, *Phys. Rev. Lett.* **108**, 247601 (2012).